

# Efficient simulation of the swept-waveform polarization dynamics in fiber spools and Fourier domain mode-locked (FDML) lasers

CHRISTIAN JIRAUSCHEK<sup>1,\*</sup> AND ROBERT HUBER<sup>2</sup>

<sup>1</sup>Institute for Nanoelectronics, Technical University of Munich, D-80333 Munich, Germany

<sup>2</sup>Institut für Biomedizinische Optik, Universität zu Lübeck, D-23562 Lübeck, Germany

\*Corresponding author: [jirauschek@tum.de](mailto:jirauschek@tum.de)

Journal reference: *J. Opt. Soc. Am. B* 34, 1135–1146 (2017)

We present a theoretical model and its efficient numerical implementation for the simulation of wavelength-swept waveform propagation in fiber systems such as Fourier domain mode-locked (FDML) lasers, fully accounting for the polarization dynamics in fiber spools and further polarization dependent optical components in the setup. This approach enables us to perform long-time simulations of the FDML laser dynamics over more than 100000 cavity roundtrips, as required for some FDML configurations to ensure convergence to the steady state operating regime. The model is validated against experimental results for single propagation through a fiber spool and for stationary FDML operation. The polarization dynamics due to the fiber spool, inducing polarization-mode dispersion, bending birefringence as well as cross-phase modulation, and other optical components such as the Faraday-rotating mirror used for polarization compensation is thoroughly investigated. © 2018 Optical Society of America

**OCIS codes:** (140.3600) Lasers, tunable; (140.3430) Laser theory; (260.5430) Polarization; (260.1440) Birefringence; (320.5550) Pulses; (170.4500) Optical coherence tomography.

<https://doi.org/10.1364/JOSAB.34.001135>

## 1. INTRODUCTION

For various applications such as optical coherence tomography (OCT) [1], broadband light sources with excellent coherence properties are needed. These seemingly contradicting requirements can be fulfilled by swept laser sources, performing fast narrowband frequency sweeps over a wide spectral range. However, conventional tunable laser sources are inherently limited in their sweep speed due to the required buildup time of lasing in the cavity [2]. In 2006, Fourier domain mode locking (FDML) was discovered as a new stationary operating regime, which circumvents this limitation and thus enables very high sweep rates [3]. The wavelength sweeps are here introduced by driving an intracavity bandpass filter synchronously to the roundtrip time of the circulating optical field in the laser cavity. To obtain a sufficiently large roundtrip time adapted to the tuning rate of the bandpass filter, FDML lasers require cavity lengths of up to a few km, which is achieved by using a fiber ring resonator.

For FDML lasers, a sweep range of 284 nm has been demonstrated using two semiconductor optical amplifiers (SOAs) arranged in a parallel configuration [4]. Employing the so-called buffering technique where the sweep rate is increased by com-

binning time-delayed copies of a wavelength sweep [5], sweep rates of up to 5.2 MHz have been achieved [6, 7]. Furthermore, output powers of around 100 mW have been obtained [8]. Typical instantaneous linewidths are below 0.1 nm, corresponding to a coherence length of up to centimeters [9]. This unique combination of properties makes the FDML laser the system of choice for many high speed OCT and sensing applications.

FDML-based OCT systems have been employed for various applications such as noninvasive imaging of the human retina for identifying pathologies [7], and their potential for monitoring of therapy as well as early stage cancer detection with OCT-based endomicroscopy has been demonstrated [10]. Furthermore, FDML sources are very attractive for high speed sensing applications. In particular, FDML-based fiber Bragg grating sensor systems, as used for temperature, pressure, position and vibration measurements, have shown superior performance [11–13]. A very recent FDML-based application is high speed stimulated Raman scattering spectroscopy and microscopy, enabling quantitative chemical analysis of unknown samples and label-free biomedical imaging, respectively [14]. Furthermore, the temporal compressibility of the wavelength-swept FDML output to optical pulses with durations of a few tens ps has been demonstrated, offering a new approach to ultra-

short optical pulse generation [15].

If no polarization maintaining (PM) optical components such as special PM fiber are used, polarization effects greatly influence the FDML operating characteristics due to effects such as cross-phase modulation, bending birefringence and polarization-mode dispersion (PMD) in the fiber spool [16, 17]. Theoretical models for FDML lasers typically do not take into account the polarization degree of freedom of the optical field [2, 18–21], and are thus only suitable for PM FDML setups. In this case, polarization is controlled by using PM optical fiber and other components along with spliced fiber connections to ensure accurate orientation of the optical axes [16]. Consequently, linearly polarized output is generated, which makes PM FDML lasers suitable for use in polarization sensitive OCT applications [22–24]. On the other hand, the need for PM components and spliced connections renders the setup more expensive. For this reason, commonly non-PM FDML configurations are used [6, 7, 10, 15], which are cheaper and easier to build. In these configurations, the polarization state of the optical field changes in an uncontrolled manner, which can be suppressed by using a polarization controller and a single-polarization SOA [16].

In [17], our well-established model equations for PM FDML lasers [18, 25, 26] have been extended to account for the polarization dynamics in the fiber spool and the other non-PM laser components. The large number of several million numerical grid points necessary for sufficient temporal and spectral resolution, combined with the necessity to simulate over  $10^4 - 10^5$  roundtrips to obtain convergence, requires a highly efficient numerical approach. Here, we give a detailed discussion of our polarization sensitive FDML model, and present a computationally efficient implementation. In comparison with [17] the model has been considerably refined, among other things, to include a significantly enhanced implementation of PMD with full frequency dependence. The obtained theoretical approach is used to analyze polarization effects in a fiber spool and in an FDML laser setup.

The paper is organized as follows: In Section 2, the setup of a typical non-PM FDML laser is discussed. Section 3 introduces the theoretical model for non-PM FDML lasers, and in Section 4, an efficient numerical implementation is developed. In Section 5, the model is validated against experimental results for single propagation through a fiber spool and for stationary FDML operation. Furthermore, the influence of the individual polarization effects is theoretically assessed. The paper is concluded in Section 6.

## 2. NON-POLARIZATION MAINTAINING FDML LASER SETUP

The most widely used type of FDML setup is a non-PM configuration with a broadband single-polarization SOA, which typically exhibits high gain and is available for a wide range of wavelength specifications. Here, the outcoupled light shows good linear polarization similar to the PM FDML design [16], but the polarization state has to be adjusted using a polarization controller to obtain good performance over the whole sweep range. Conventional FDML-based OCT applications typically use this type of FDML setup [6, 7, 10], and also polarization sensitive OCT has already been demonstrated with such a design [27].

Non-PM setups with polarization insensitive SOA can be used for applications which are not polarization dependent.

In contrast to non-PM setups with single-polarization SOAs, no adjustment of the polarization controller is required to obtain good performance. However, the polarization state significantly changes over the sweep and furthermore exhibits large sweep-to-sweep fluctuations [16]. Moreover, polarization insensitive broadband SOAs tend to have a lower gain than their polarization dependent counterparts, and for certain wavelength ranges they are not available. On the other hand, preliminary results indicate that non-PM FDML configurations with polarization insensitive SOA have a smaller linewidth, which is tentatively attributed to self-regulation effects using the polarization degree of freedom [17]. Recently, the excellent coherence properties of such setups have even been exploited to generate picosecond pulses by external compression of the wavelength sweeps [15]. The potential to control the pulse shape by adapting the sweep filter drive waveform and the SOA current, as well as optical pulse energies in the  $\mu\text{J}$  range, make this concept appealing. In Fig. 1, a non-PM FDML laser

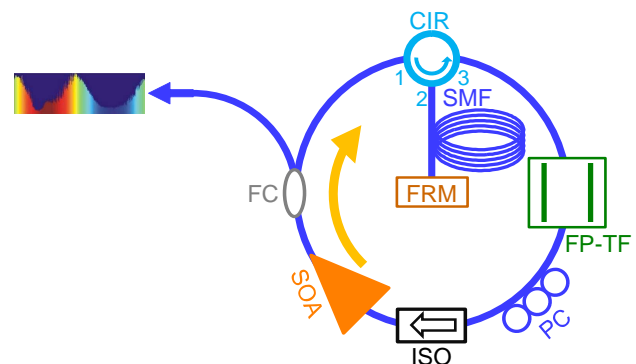


**Fig. 1.** Schematic illustration of a non-polarization maintaining FDML laser setup.

setup is schematically illustrated. As a gain medium, an SOA is used, followed by a fiber output coupler (FC) where part of the light is outcoupled. To ensure unidirectional lasing, an optical isolator (ISO) is built in before the SOA. Using a circulator (CIR), the light is coupled into a single-mode fiber (SMF) spool serving as a delay line. The effective cavity length is doubled by back-reflecting the light at the fiber end. For this purpose, a Faraday rotating mirror (FRM) is used which also rotates the polarization angle by  $90^\circ$  to achieve a partial compensation of polarization effects in the optical fiber. A Fabry-Pérot tunable filter (FP-TF) with a bandwidth of typically  $\sim 0.15\text{ nm}$  serves for wavelength selection, while the instantaneous linewidth of the laser light is considerably narrower. Rapid wavelength tuning is here achieved by synchronizing the tuning rate of the FP-TF to the optical roundtrip time of light circulating in the laser cavity, which avoids repeated build-up of the optical resonator field.

## 3. THEORETICAL MODEL

Important fiber propagation effects are self-phase modulation (SPM) due to an intensity dependent refractive index and dispersion due to the dependence of the propagation constant  $\beta$  on the (angular) frequency  $\omega$ . Commonly,  $\beta$  is represented by its Taylor series about the center frequency  $\omega_c$  of the optical field,

$$\beta(\omega) = \sum_j (\omega - \omega_c)^j \beta^{(j)} / j!, \quad (1)$$

with  $\beta^{(j)} = \partial_{\omega}^j \beta(\omega_c)$ . The polarization effects in the optical fiber are mainly related to birefringence, causing different phase and group velocities for the electric field components  $E_{x,y}$  in the two polarization directions  $x$  and  $y$ , i.e.,  $\beta_x^{(0)} \neq \beta_y^{(0)}$  and  $\beta_x^{(1)} \neq \beta_y^{(1)}$ . Bending birefringence is due to lateral internal stress in bent optical fibers, such as fibers wound on a spool or fiber loops used for polarization control. Besides, imperfections such as anisotropic stresses and deviations from rotational symmetry lead to additional birefringence contributions which vary along the fiber, giving rise to PMD. The modeling of this effect poses an extra challenge due to the random nature of the imperfections, requiring a stochastic treatment. The nonlinear birefringence contribution accompanying SPM leads to coupling between the two field polarization components, which is referred to as cross-phase modulation (XPM).

We describe the optical field by its slowly varying envelope functions  $A_{x,y}(z, \tau)$ , defined so that  $E_{x,y} \propto \Re \left\{ A_{x,y} \exp \left[ i \left( \beta_x^{(0)} + \beta_y^{(0)} \right) z/2 - i\omega_c \tau \right] \right\}$  and the optical power is  $|A_x|^2 + |A_y|^2$ , where  $z$  is the propagation coordinate in the laser system and  $\tau$  represents the time variable. Introducing the retarded time  $t = \tau - \left( \beta_x^{(1)} + \beta_y^{(1)} \right) z/2$  defined with respect to a frame moving along with the optical field, propagation through an optical fiber system can be described by coupled nonlinear Schrödinger equations for the two polarization components [28],

$$\begin{aligned} \partial_z A_{x,y} = & \left[ \pm \frac{i}{2} \Delta_{\beta,b} (\omega_c + i\partial_t) + i \sum_{j \geq 2} D_j (i\partial_t)^j \right] A_{x,y} \\ & + i\gamma \left( |A_{x,y}|^2 + \frac{2}{3} |A_{y,x}|^2 \right) A_{x,y} \\ & + [g_{x,y} (\omega_c + i\partial_t) (1 - i\alpha) - a_{x,y} (\omega_c + i\partial_t)] A_{x,y} \\ & + \frac{i}{2} \Delta_{\beta,\text{PMD}} (\omega_c + i\partial_t) [\pm \cos(\theta) A_{x,y} + \sin(\theta) A_{y,x}]. \end{aligned} \quad (2)$$

The first line contains birefringence and dispersion effects, where  $\Delta_{\beta,b} = \beta_x - \beta_y$  denotes the difference of the propagation constants for the two polarization directions due to bending birefringence, see Section 3 A. Since  $\beta$  is a function of  $\omega$ , see Eq. (1), also  $\Delta_{\beta,b}$  is frequency dependent, which is in time domain reflected by the operator function  $\Delta_{\beta,b}(\omega_c + i\partial_t)$ . The second line contains SPM and XPM. Chromatic dispersion, characterized by  $j$ th order dispersion coefficients  $D_j = \beta^{(j)}/j!$  with  $j = 2, 3, \dots$ , as well as the nonlinear coefficient  $\gamma$  describing SPM and XPM, is assumed to be identical for both polarization directions [28]. The third line describes frequency dependent amplitude gain and loss, represented by separate coefficients  $g_{x,y}(\omega)$  and  $a_{x,y}(\omega)$  for the two polarization directions to account for the polarization sensitivity of optical components such as the SOA module. Linewidth enhancement of the SOA is taken into account by the Henry factor  $\alpha$ , and gain saturation is modeled by introducing an optical power dependence into  $g_{x,y}$  [18, 26]. In the fourth line, PMD in the fiber is implemented according to [29, 30]. In this approach, the random nature of PMD is reflected by fixed PMD-related birefringence contributions  $\Delta_{\beta,\text{PMD}}$  at randomly varying orientation angles  $\theta$  with  $\partial_z \theta = g_{\theta}(z)$ . Here,  $g_{\theta}(z)$  is a white noise process with  $\langle g_{\theta}(z) \rangle = 0$ ,  $\langle g_{\theta}(z) g_{\theta}(z') \rangle = 2h_f^{-1} \delta(z - z')$ , and  $h_f$  denotes the fiber autocorrelation length [29, 30].

The number of required simulation grid points for sufficient temporal and spectral resolution is set by the time-bandwidth product of the field components  $A_{x,y}$ , which in FDML lasers corresponds to the product of the sweep bandwidth and cavity roundtrip time, typically  $\sim 10 \text{ THz} \times 10 \mu\text{s} = 10^8$ . This impedes a direct numerical evaluation of Eq. (2). The computational load can be considerably reduced by introducing a sliding spectral reference frame moving along with the time dependent center frequency  $\Omega(t)$  of the sweep filter, and transforming  $A_{x,y}$  to the swept filter reference frame [18], with

$$u_{x,y}(z, t) = A_{x,y}(z, t) \exp \left\{ i \int^t [\Omega(t') - \omega_c] dt' \right\}. \quad (3)$$

Inserting Eq. (3) into Eq. (2) and approximating  $\partial_t^j A_{x,y} \approx [-i(\Omega - \omega_c)]^j u_{x,y}$ , i.e., neglecting higher order terms [18], yields

$$\begin{aligned} \partial_z \mathbf{u} = & \left[ i \sum_{j \geq 2} D_j (\Omega - \omega_c)^j + i\gamma \begin{pmatrix} |u_x^2| & 0 \\ 0 & |u_y^2| \end{pmatrix} - a_s(i\partial_t) \right. \\ & + \begin{pmatrix} g_x(\Omega) & 0 \\ 0 & g_y(\Omega) \end{pmatrix} (1 - i\alpha) - \begin{pmatrix} a_x(\Omega) & 0 \\ 0 & a_y(\Omega) \end{pmatrix} \\ & + \frac{i}{2} \Delta_{\beta,\text{PMD}}(\Omega) \begin{pmatrix} \cos \theta & \sin \theta \\ \sin \theta & -\cos \theta \end{pmatrix} \\ & \left. + i\frac{2}{3} \gamma \begin{pmatrix} |u_y^2| & 0 \\ 0 & |u_x^2| \end{pmatrix} + \frac{i}{2} \Delta_{\beta,b}(\Omega) \begin{pmatrix} 1 & 0 \\ 0 & -1 \end{pmatrix} \right] \mathbf{u}, \end{aligned} \quad (4)$$

where  $\mathbf{u} = [u_x, u_y]^T$  and T denotes the transpose. In this new reference frame, the sweep filter can simply be described by its static bandpass characteristics, here represented by a frequency dependent loss coefficient  $a_s(\omega)$  centered at  $\omega = 0$ . In time domain, this corresponds to an operator function  $a_s(i\partial_t)$ . This implies that even for a rapidly wavelength-tuned filter acting on a suitably wavelength-swept optical field, the field “sees” a stationary bandpass filter in the swept filter reference frame, as has been verified by an exact treatment based on Maxwell’s equations [2]. The transformed spectrum is now limited by the sweep filter bandwidth rather than the sweep range, reducing the number of required grid points by about two to three orders of magnitude. Setting  $g_x = g_y = g$  and  $a_x = a_y = a$ , the first and second line of Eq. (4) correspond to the previously developed FDML model without polarization effects [18, 25, 26]. The third and fourth line contain fiber polarization effects due to PMD, XPM and bending birefringence. The used models for  $\Delta_{\beta,b}$  and  $\Delta_{\beta,\text{PMD}}$  are discussed in Sections 3 A and 3 B, respectively.

In Fig. 2, the FDML model employed for simulating non-PM laser setups as shown in Fig. 1 is schematically illustrated. Here, the subsystem consisting of the circulator, fiber spool and FRM is unfolded, taking advantage of the fact that the interaction of the forward and backward propagating light in the fiber can be neglected. All the parameters depend on the position  $z$ ; for example, the coefficients  $g_{x,y}$  are non-zero only inside the gain medium. A self-consistent laser model requires the inclusion of saturation effects, as can be done by introducing power dependent gain coefficients. Besides SOAs, for example also erbium-doped and Raman fiber gain media have been employed for FDML lasers [31, 32], and the details of the gain model depend on the type of optical amplifier

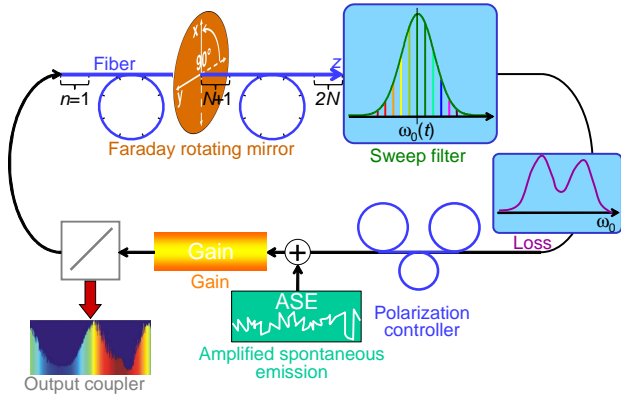


**Fig. 2.** Schematic diagram of the FDML model used for the simulation of the laser setup sketched in Fig. 1.

used. The sweep filter is modeled as a lumped component, described by a complex Lorentzian amplitude transmission profile  $t_s(\omega) = \exp[-\int a_s(\omega) dz] = T_{\max}^{1/2} / (1 - 2i\omega/\Delta_s)$  with the full width at half-maximum (FWHM) bandwidth  $\Delta_s$  and peak transmittance  $T_{\max}$  [2, 18, 26]. In addition to the effects included in Eq. (4), amplified spontaneous emission (ASE) in the gain medium is considered by an equivalent noise source at the input of the gain medium [18, 26, 33]. Furthermore, the Faraday rotating mirror at the end of the fiber spool is modeled as discussed in Section 3C. The polarization controller consists of three fiber loops which are twisted against each other. This allows for an adjustment of the polarization state by exploiting bending birefringence in the loops, already included in Eq. (4). The resulting model equations for the polarization controller are derived in Section 3D.

### A. Bending Birefringence

For a fiber with a cladding radius  $r$  and a bending radius  $R_b$ , the bending-induced difference between the propagation constants of the two axes is given by [34, 35]

$$\begin{aligned} \Delta_{\beta,b} &= \beta_x - \beta_y = \omega c^{-1} n_0^3 (1 + \nu) (p_{11} - p_{12}) (r/R_b)^2 / 4 \\ &= -\omega c^{-1} EC (r/R_b)^2 / 2, \end{aligned} \quad (5)$$

where  $x$  indicates the component in the direction of the bending radius, and  $y$  is the component orthogonal to the coil plane. Furthermore,  $\nu$  is Poisson's ratio,  $p_{11}$  and  $p_{12}$  are elements of the photoelastic tensor in silica,  $n_0$  is the refractive index, and  $c$  denotes the vacuum speed of light. Young's modulus  $E$  is a purely mechanical constant and thus wavelength independent, with  $E = 72.7$  GPa for fused silica [36]. The dependence of the relative optoelastic constant  $C$  on the vacuum wavelength  $\lambda = 2\pi c/\omega$  is for single-mode silica fibers given by the empirical equation  $C \approx \sum_{\ell=0}^3 C_\ell (\lambda/\mu\text{m})^\ell \times 9.80665^{-1} \times 10^{-5} \text{ mm}^2/\text{N}$  with  $C_0 = 3.95065$ ,  $C_1 = -1.72552$ ,  $C_2 = 1.52460$ ,  $C_3 = -0.50708$ , extracted from measurements of  $C$  for wavelengths  $0.6 \mu\text{m} < \lambda < 1.6 \mu\text{m}$  [35]. The factor  $9.80665^{-1}$  has been added to convert from the units  $\text{mm}^2/\text{kg}$  used in [35] to the units used here. With Eq. (5), we obtain

$$\begin{aligned} \Delta_{\beta,b}(\omega) &= \left[ -0.488 \left( \omega/\text{fs}^{-1} \right) + 0.402 - 0.669 \left( \omega/\text{fs}^{-1} \right)^{-1} \right. \\ &\quad \left. + 0.419 \left( \omega/\text{fs}^{-1} \right)^{-2} \right] (r/R_b)^2 \times 10^6 \text{ m}^{-1}. \end{aligned} \quad (6)$$

The optical fibers used in the fiber spool and FDML laser setup investigated here have a cladding radius  $r = 62.5 \mu\text{m}$  [37].

### B. Polarization-mode dispersion

PMD in a fiber is usually characterized in terms of the PMD parameter  $D_p$  and fiber autocorrelation length  $h_f$  at the frequency of interest  $\omega_c$  [28]. From these quantities, the first order derivative of  $\Delta_{\beta,\text{PMD}}$  is obtained as [28]

$$\frac{d}{d\omega} \Delta_{\beta,\text{PMD}} = \Delta'_{\beta,\text{PMD}} = D_p (2h_f)^{-1/2}. \quad (7)$$

For our FDML model, Eq. (4), the knowledge of  $\Delta'_{\beta,\text{PMD}}$  and  $h_f$  is not sufficient, but rather the dependence of  $\Delta_{\beta,\text{PMD}}$  on  $\omega$  must be known over the full sweep bandwidth, which can be obtained from a suitable physical model. PMD in single-mode optical fibers is due to imperfections introduced during manufacturing, such as a noncircular core giving rise to geometry-related and stress-related birefringence. The latter is caused by non-symmetrical stress, which builds up during the cooling process due to deviations from the circular fiber geometry, and dominates for fibers with small index contrast [38]. Using the frequency dependent expression for  $\Delta_{\beta,b}(\omega)$  given in Eq. (5), the stress birefringence can be written as [38]

$$\begin{aligned} \Delta_{\beta,\text{PMD}} &= \varepsilon \frac{(a_1 - a_2)(T_r - T_s)}{(1 - \nu)} \left( \frac{R_b}{r} \right)^2 \Delta_{\beta,b}(\omega) F(\omega), \\ F(\omega) &= \frac{W^2}{V^2} - 3 \frac{a_c^4}{r^4} + \frac{a_c^6}{r^6} \left[ 2 + \frac{4(U^2 - W^2)}{U^2 W^2} + \frac{4 J_0(U)}{U J_1(U)} \right]. \end{aligned} \quad (8)$$

Here,  $V = a_c \omega c^{-1} n_0 (2\Delta)^{1/2}$  is the normalized frequency,  $W$  is approximately given by  $W \approx 1.1428V - 0.9960$  (with an error  $< 0.1\%$  for  $1.5 \leq V \leq 2.5$ ) [39], and  $U = (V^2 - W^2)^{1/2}$ . The  $J_n$  are Bessel functions of the first kind. For an SMF-28 single-mode fiber, we have an (average) core radius of  $a_c = 4.1 \mu\text{m}$  and a refractive index difference between core and cladding of  $\Delta = 0.0036$  [37]. Furthermore,  $\varepsilon$ ,  $a_{1,2}$ ,  $T_{r,s}$  and  $\nu$  denote the core ellipticity, thermal expansion coefficients of the core and cladding, room temperature and glass softening temperature, and Poisson's ratio, respectively. It is practical to rewrite Eq. (8) by using Eq. (7), which gives

$$\Delta_{\beta,\text{PMD}} = \Delta'_{\beta,\text{PMD}}(\omega_c) \frac{\Delta_{\beta,b}(\omega) F(\omega)}{\frac{d}{d\omega} [\Delta_{\beta,b}(\omega) F(\omega)] \Big|_{\omega=\omega_c}}. \quad (9)$$

For our simulations, we assume typical values of  $D_p = 0.05 \text{ ps/km}^{1/2}$  and  $h_f = 10 \text{ m}$  [28, 37], yielding with Eq. (7)  $\Delta'_{\beta,\text{PMD}} = 0.354 \text{ ps/km}$ .

### C. Faraday Rotating Mirror

As shown in Fig. 1, the Faraday rotating mirror (FRM) back-reflects the light at the end of the fiber spool with a polarization angle rotated by  $90^\circ$ . Ideally, this results in a compensation of polarization effects in the spool, at least for low power levels where nonlinear optical effects due to SPM and XPM are negligible. In practice, a  $90^\circ$  rotation is only obtained at the FRM design wavelength  $\lambda_F$ , preventing a full compensation of the polarization effects over the complete wavelength sweep range. Thus, we use a more realistic model of the FRM, allowing us to capture these residual effects. The FRM utilizes the Faraday

effect where a magnetic field of strength  $B$  in the optical propagation direction causes a rotation of the polarization angle by  $\phi = BV_F L_F$ , with the Verdet constant of the material  $V_F$  and the total path length of the light  $L_F$  [40]. For a paramagnetic material,  $V_F$  is expected to depend on the wavelength  $\lambda$  according to  $V_F = \Xi / (\lambda^2 - \lambda_r^2)$ , where  $\lambda_r$  denotes the wavelength corresponding to the ultraviolet resonance peak and  $\Xi$  is a material constant [41]. For the FDML laser, the wavelength of the light field is determined by the center wavelength of the sweep filter,  $\lambda = 2\pi c / \Omega$ . Using  $\phi = B\Xi L_F / (\lambda_F^2 - \lambda_r^2) = \pi/2$  at the design wavelength  $\lambda_F$ , we obtain

$$\phi(\Omega) = \frac{\pi}{2} \frac{\lambda_F^2 - \lambda_r^2}{(2\pi c / \Omega)^2 - \lambda_r^2}. \quad (10)$$

Thus the field envelope  $\mathbf{u}$  defined in Eq. (3) is transformed according to  $\mathbf{u}_{\text{out}}(t) = M_{\text{FRM}}(t) \mathbf{u}_{\text{in}}(t)$  with

$$M_{\text{FRM}}(t) = \sqrt{R} \begin{pmatrix} \cos\{\phi[\Omega(t)]\} & -\sin\{\phi[\Omega(t)]\} \\ \sin\{\phi[\Omega(t)]\} & \cos\{\phi[\Omega(t)]\} \end{pmatrix}, \quad (11)$$

where the insertion loss of the FRM is captured by the power reflectance  $R$ .

Here we use a value  $\lambda_r = 363$  nm, which has been obtained by a fit to experimental data for terbium gallium garnet [41]. This value also describes well experimental data for other materials used for FRMs, such as rare-earth iron garnet [42] as well as terbium-doped glass [43]. In the following, we assume an insertion loss of 1 dB [44], corresponding to  $R \approx 0.80$ .

#### D. Polarization Controller

The polarization controller (PC) consists of three paddles, i.e., fiber coils with diameters of several cm and multiple windings. These coils are chosen so that a phase shift between the two polarization components of  $\pi/2$ ,  $\pi$  and again  $\pi/2$  is obtained, corresponding to a  $\lambda/4$ ,  $\lambda/2$  and  $\lambda/4$  waveplate, respectively [16]. Each paddle can be tilted, so that the principal polarization axes are rotated against each other. In experiment, the PC is manually adjusted until good lasing is obtained, which can be achieved for different settings [16]. In our model, the PC setting is described by three orientation angles  $\phi_i$  ( $i = 1, 2, 3$ ) for the principal polarization axes of the three coils, where we assume that the associated twisting of the fiber is a second order effect which can be neglected. Due to the relatively short fiber length in the PC, we neglect PMD, fiber nonlinearities and dispersion in Eq. (4), only considering the bending birefringence term. Thus, we obtain for a single coil with fiber length  $L_c$  the solution  $\mathbf{u}_{\text{out}} = M \mathbf{u}_{\text{in}}$  with

$$M(\Omega) = \begin{pmatrix} \exp\left[\frac{i}{2}\Delta_{\beta,b}(\Omega)L_c\right] & 0 \\ 0 & \exp\left[-\frac{i}{2}\Delta_{\beta,b}(\Omega)L_c\right] \end{pmatrix}, \quad (12)$$

where  $\Delta_{\beta,b}(\Omega)$  is given by Eq. (6). The matrices  $M_{\lambda/4}$  and  $M_{\lambda/2}$  for the quarter- and half-waveplate fiber coil are obtained from Eq. (12) by setting  $L_c = \left|\Delta_{\beta,b}^{-1}(\omega_c)\right| \pi/2$  and  $L_c = \left|\Delta_{\beta,b}^{-1}(\omega_c)\right| \pi$ , respectively. With the rotation matrix

$$M(\phi) = \begin{pmatrix} \cos\phi & -\sin\phi \\ \sin\phi & \cos\phi \end{pmatrix},$$

the total matrix of the polarization controller is obtained as

$$M_{\text{PC}}(t) = M(\phi_3) M_{\lambda/4}[\Omega(t)] M(\phi_2 - \phi_3) M_{\lambda/2}[\Omega(t)] \\ \times M(\phi_1 - \phi_2) M_{\lambda/4}[\Omega(t)] M(-\phi_1). \quad (13)$$

#### 4. NUMERICAL IMPLEMENTATION

The simulation of the FDML dynamics is based on numerically solving Eq. (4). Here, the sweep filter term is evaluated in Fourier domain, while the other effects are treated in time domain. The temporal simulation window is adapted to the roundtrip time in the laser cavity, taking advantage of the implicit periodic boundary conditions of the numerical scheme [18, 26]. The implementation of the SOA is discussed in Section 5B.

The computationally expensive part is computing the optical propagation through the fiber spool, where the stochastic nature of PMD is reflected by a randomly varying orientation angle  $\theta$  with  $\partial_z \theta = g_\theta(z)$  as described in Section 3. Here,  $g_\theta(z)$  is a white noise process with  $\langle g_\theta(z) \rangle = 0$  and  $\langle g_\theta(z) g_\theta(z') \rangle = 2h_f^{-1} \delta(z - z')$  where  $h_f$  denotes the fiber autocorrelation length [29, 30]. This effect is numerically implemented by dividing the fiber into a large number of small segments of length  $d$ , chosen so that  $d \ll h_f$ . The orientation angle in each segment  $n$  is then randomly chosen using

$$\theta_n = \theta_0 + (2d/h_f)^{1/2} \sum_{\ell=1}^n x_\ell, \quad (14)$$

where  $\theta_0$  is a random variable uniformly distributed on  $[0, 2\pi]$ , and the  $x_\ell$  are independent random variables distributed according to the standard normal distribution  $f(x_\ell) = (2\pi)^{-1/2} \exp(-x_\ell^2/2)$ . For the simulation, the experimental sigma ring geometry shown in Fig. 1 is replaced by an equivalent unfolded configuration with unidirectional propagation through the optical fiber, see Fig. 2. As described in Section 2, partial compensation of the polarization effects in the fiber spool is experimentally achieved by back-reflecting the light with  $90^\circ$  rotated polarization. In our simulation, this is considered by mirror symmetry of the fiber with respect to the FRM in the unfolded configuration. Thus, in the simulation the PMD orientation angles  $\theta_n$  of the fiber segments  $n = 1 \dots N$  to the left of the FRM in Fig. 2 are randomly chosen, and the angles of the mirror segments  $n = (N+1) \dots 2N$  to the right of the FRM are given by  $\theta_n = \theta_{2N+1-n}$ . Eq. (4) can then be solved numerically based on an analytical solution for each segment.

For the propagation of optical pulses in a fiber of length  $L$ , the time delay  $\Delta T$  between the two polarization components due to PMD depends on the random changes in birefringence, with the variance of  $\Delta T$  given by  $\sigma_{\Delta T}^2 \approx D_p^2 h_f [\exp(-L/h_f) + L/h_f - 1]$  [28]. Our PMD implementation based on randomly chosen birefringence orientation angles, Eq. (14), was validated against this analytical model for different fiber parameters by propagating Gaussian optical pulses for many stochastic realizations of  $\theta$ , and computing  $\sigma_{\Delta T}^2$  from the obtained distribution of  $\Delta T$ .

In an optical fiber, we have  $a_s = 0$ , and typically identical loss for both polarization directions,  $a_x = a_y =: a$  [28]. Furthermore assuming no fiber gain,  $g_{x,y} = 0$ , the solution of the linear part of Eq. (4), i.e., without SPM and XPM, is for segment  $n$  at

$z_n \leq z < z_n + d$  given by

$$\begin{pmatrix} u_x(z_n + d, t) \\ u_y(z_n + d, t) \end{pmatrix} = \exp \left\{ i \sum_{j \geq 2} [\Omega(t) - \omega_c]^j D_j d - ad \right\} \times M_{L,n}(t) \begin{pmatrix} u_x(z_n, t) \\ u_y(z_n, t) \end{pmatrix}. \quad (15)$$

$\Omega(t)$  is determined by the output waveform of the function generator used to drive the sweep filter. For example, sinusoidal modulation can be applied, yielding  $\Omega(t) = \omega_c + (\Delta\omega/2) \cos(2\pi t/T_R)$  with the cavity roundtrip time  $T_R$  and sweep range  $\Delta\omega$ . The matrix  $M_{L,n}$ , like the matrices  $M_{FRM}$  and  $M_{PC}$  defined in Eqs. (11) and (13), has the form

$$M = \begin{pmatrix} A & B \\ -B^* & A^* \end{pmatrix}, \quad (16)$$

where the asterisk denotes the complex conjugate and the matrix elements are given by

$$\begin{aligned} A_{L,n}(t) &= \cos \left\{ \frac{d}{2} \Delta_{\beta,n} [\Omega(t)] \right\} \\ &+ i \frac{\Delta_{\beta,b} [\Omega(t)] + \Delta_{\beta,PMD} [\Omega(t)] \cos \theta_n}{\Delta_{\beta,n} [\Omega(t)]} \sin \left\{ \frac{d}{2} \Delta_{\beta,n} [\Omega(t)] \right\}, \\ B_{L,n}(t) &= i \frac{\Delta_{\beta,PMD} [\Omega(t)]}{\Delta_{\beta,n} [\Omega(t)]} \sin \left\{ \frac{d}{2} \Delta_{\beta,n} [\Omega(t)] \right\} \sin \theta_n. \end{aligned} \quad (17)$$

$\Delta_{\beta,b}(\Omega)$  and  $\Delta_{\beta,PMD}(\Omega)$  are defined in Eq. (6) and Eq. (9), respectively, and  $\Delta_{\beta,n} = \left( \Delta_{\beta,b}^2 + \Delta_{\beta,PMD}^2 + 2\Delta_{\beta,b}\Delta_{\beta,PMD} \cos \theta_n \right)^{1/2}$ .

The nonlinear part of Eq. (4) containing SPM and XPM can be rearranged as

$$\partial_z \mathbf{u}|_{NL} = i\gamma \left[ \frac{5}{6} \left( |u_x^2| + |u_y^2| \right) + \frac{1}{6} \left( |u_x^2| - |u_y^2| \right) \begin{pmatrix} 1 & 0 \\ 0 & -1 \end{pmatrix} \right] \mathbf{u}. \quad (18)$$

The solution is given by

$$\begin{pmatrix} u_x(z_n + d, t) \\ u_y(z_n + d, t) \end{pmatrix} = \exp \left\{ i \frac{5}{6} \gamma \left[ |u_x^2(z_n, t)| + |u_y^2(z_n, t)| \right] d \right\} \times M_{NL,n}(t) \begin{pmatrix} u_x(z_n, t) \\ u_y(z_n, t) \end{pmatrix}, \quad (19)$$

where  $M_{NL,n}$  again assumes the form Eq. (16) with

$$\begin{aligned} A_{NL,n}(t) &= \exp \left\{ i \frac{\gamma d}{6} \left[ |u_x^2(z_n, t)| - |u_y^2(z_n, t)| \right] \right\}, \\ B_{NL,n}(t) &= 0. \end{aligned} \quad (20)$$

The total matrix for the fiber spool with the FRM can then be obtained by subsequently propagating the field vector  $\mathbf{u}$  through the fiber segments  $n = 1 \dots N$ , the FRM, Eq. (11), and again the fiber segments in reverse order. The linear and nonlinear effects are evaluated separately for each fiber segment using Eqs. (15) and (19), respectively, where the  $|u_x^2|$  and  $|u_y^2|$  in Eq. (19) have to be updated for each propagation step.

The fiber loss can in FDML lasers usually be neglected, corresponding to  $a \approx 0$ . Then the total optical power does not change along the fiber, i.e.,  $|u_x^2(z, t)| + |u_y^2(z, t)| = |u_x^2(0, t)| + |u_y^2(0, t)| = P(t)$  for the fiber section in Fig. 2 before the FRM, and

$$P_{\text{out}}(t) = R \left( |u_x^2(0, t)| + |u_y^2(0, t)| \right) = RP(t) \quad (21)$$

for the section after the FRM. Under this condition, the output field  $\mathbf{u}_{\text{out}}$  of the delay line, consisting of the fiber spool with length  $L$  and FRM, is related to the input field  $\mathbf{u}(0)$  by

$$\begin{aligned} \mathbf{u}_{\text{out}}(t) &= \exp \left\{ i \frac{5}{6} \gamma \left[ |u_x^2(0, t)| + |u_y^2(0, t)| \right] L (1 + R) \right\} \\ &\times \exp \left\{ 2iL \sum_{j \geq 2} [\Omega(t) - \omega_c]^j D_j \right\} M_{FS}(t) \mathbf{u}(0, t), \end{aligned} \quad (22)$$

with the total matrix

$$M_{FS} = M_{2N} M_{2N-1} \dots M_{N+1} M_{FRM} M_N \dots M_1, \quad (23)$$

where  $M_n = M_{NL,n} M_{L,n}$  with  $M_{NL,n}$  and  $M_{L,n}$  given by Eqs. (20) and (17), respectively. Furthermore,  $\theta_{2N+1-n} = \theta_n$  in Eq. (17) as discussed above, which results in  $M_{L,2N+1-n} = M_{L,n}$ . The accuracy of this split-step approach can be improved by adopting a symmetrized procedure [28]. Here, the nonlinear effects are evaluated in the middle of the segments, i.e., the matrix Eq. (17) describing the linear effects is divided into two identical parts  $M_{L,n}(d/2)$  for half the segment width  $d/2$ , yielding the matrix  $M_{L,n}(d/2) M_{NL,n}(d) M_{L,n}(d/2)$  for segment  $n$ .

The matrices  $M_{FRM}$ ,  $M_{L,n}$  and  $M_{NL,n}$  defined in Eqs. (11), (17) and (20), as well as the matrix representing the polarization controller  $M_{PC}$  given by Eq. (13), are all of the form Eq. (16). Products of such matrices also assume the form Eq. (16), which can be exploited to reduce the numerical effort for matrix multiplication since only the matrix elements in the upper row must be determined.

## A. Evaluation of the Fiber Nonlinearity

Typically the temporal simulation window has to be resolved by several million grid points for sufficient temporal and spectral resolution. Furthermore, the optical field is propagated over several  $10^4$  roundtrips to obtain convergence. Thus, the fiber propagation matrix  $M_{FS}$ , Eq. (23), has to be precomputed and stored for each sweep filter frequency value  $\Omega(t_m)$  associated with a temporal grid point  $t_m$ . In addition, the dependence of Eq. (23) on  $|u_x^2| - |u_y^2|$ , which is introduced by the  $M_{NL,n}$  defined in Eq. (20), must be considered. This can be done by precomputing  $M_{FS}$  at each  $\Omega(t_m)$  for different values  $|u_x^2| - |u_y^2|$  which are then used for interpolation.

In the following, we derive a suitable interpolation function. As pointed out above, all the matrices in Eq. (23), and thus also any product of these matrices, have the form Eq. (16), so that the  $|u_{x,y}^2|$  for  $M_{NL,n}$  in Eq. (20) can be expressed as  $|u_x| = |Au_x(0) + Bu_y(0)|$ ,  $|u_y| = |-B^*u_x(0) + A^*u_y(0)|$ , where we have dropped the  $t$  dependence for notational convenience. Writing  $u_x(0) = P^{1/2} \exp(i\rho_x) \cos \delta$ ,  $u_y(0) = P^{1/2} \exp(i\rho_y) \sin \delta$  with the optical power  $P$ , phases  $\rho_{x,y}$  and

polarization angle  $\delta$ , we express the phase term in Eq. (20) as

$$\begin{aligned}\varphi &= \frac{\gamma d}{6} \left( |u_x^2| - |u_y^2| \right) \\ &= \frac{\gamma d}{6} P \left\{ \left( |A|^2 - |B|^2 \right) \cos(2\delta) + 2\Re[BA^* \exp(i\rho) \sin(2\delta)] \right\} \\ &= PP_0^{-1} [\cos(2\delta) + \kappa (\cos\psi \cos\rho - \sin\psi \sin\rho) \sin(2\delta)],\end{aligned}\quad (24)$$

where  $P_0^{-1} = \gamma d \left( |A|^2 - |B|^2 \right) / 6$ ,  $\rho = \rho_y - \rho_x$ ,  $\psi = \angle B - \angle A$ , and  $\kappa = 2|AB| / \left( |A|^2 - |B|^2 \right)$ . For the typical parameter values in FDML lasers, we have  $|\varphi| \ll 1$  and can thus approximate  $\exp(\pm i\varphi) \approx 1 \pm i\varphi$ . Hence, Eq. (20) can be written as  $M_{\text{NL}} \approx I + \varphi \Delta_{\text{NL}}$  where the matrix  $\Delta_{\text{NL}}$  has the form Eq. (16) with  $A = i$ ,  $B = 0$ , and  $I$  denotes the unit matrix. Consequently, the power dependence of the total propagation matrix  $M_{\text{FS}}$  in Eq. (23) is to first order given by  $M_{\text{FS}}(P) = M_{\text{FS}}(P=0) + \varphi \Delta_{\text{FS}}$ , with  $\varphi$  given by Eq. (24). The unknowns which have to be determined are  $\kappa$ ,  $\psi$  and the matrix  $P_0^{-1} \Delta_{\text{FS}}$ . Alternatively, we can rewrite this expression using three dimensionless matrices  $\Delta_{1,2,3}$  of the form Eq. (16),

$$\begin{aligned}M_{\text{FS}}(P) &= M_{\text{FS}}(P=0) + PP_0^{-1} [\Delta_1 \cos(2\delta) \\ &\quad + (\Delta_2 \cos\rho + \Delta_3 \sin\rho) \sin(2\delta)].\end{aligned}\quad (25)$$

In this equation,  $P_0$  assumes the role of a reference power. Eq. (25) describes the influences of the fiber nonlinearity very accurately if  $P_0$  is set to a typical optical power level in the FDML fiber spool; here we choose  $P_0 = 100$  mW.  $M_{\text{FS}}(P=0)$  is obtained from Eq. (23) for  $u_x(0) = u_y(0) = 0$ . The  $\Delta_i$  can then be determined by computing Eq. (23) for three initial fields  $\mathbf{u}(0)$ . For example,  $u_x(0) = P_0^{1/2}$ ,  $u_y(0) = 0$ , which corresponds to  $\delta = 0$  and  $P = P_0$ , yields  $\Delta_1 = M_{\text{FS}}(P_0)|_{\delta=0} - M_{\text{FS}}(P=0)$ . Likewise,  $u_x(0) = u_y(0) = (P_0/2)^{1/2}$  yields  $\Delta_2 = M_{\text{FS}}(P_0)|_{\delta=\pi/4, \rho=0} - M_{\text{FS}}(P=0)$ , and  $u_x(0) = (P_0/2)^{1/2}$ ,  $u_y(0) = i(P_0/2)^{1/2}$  gives  $\Delta_3 = M_{\text{FS}}(P_0)|_{\delta=\pi/4, \rho=\pi/2} - M_{\text{FS}}(P=0)$ . The accuracy of this propagation matrix can be further improved by strictly enforcing the relation between output and input power given in Eq. (21). This yields the improved matrix

$$M_{\text{FS,corr}}(P) = [R / |M_{\text{FS}}(P)|]^{1/2} M_{\text{FS}}(P), \quad (26)$$

where  $|M_{\text{FS}}(P)|$  denotes the matrix determinant.

## 5. RESULTS

In the following, we use the numerical approach developed in Section 4 to simulate propagation through a fiber spool and operation of an FDML laser, respectively. Fiber bending birefringence and PMD are implemented as described in Sections 3A and 3B, respectively, and the nonlinearity is treated according to Eqs. (25) and (26). The FRM is implemented as described in Section 3C. In our simulations, we use a fiber segment length of  $d = 0.005$  m to obtain sufficient spatial resolution.

### A. Propagation through a Fiber Spool

In the following, we simulate the propagation of wavelength-swept, linearly polarized light through a fiber spool, and compare the obtained output state of polarization (SOP) to experimental results [16]. We study propagation through a 1 km spool with a bending radius  $R_b = 0.115$  m [16], where the light is

back-reflected at the fiber end using an FRM to obtain a partial compensation of polarization effects and a doubling of the propagation length. Such a system is employed in FDML lasers as a delay line, see Fig. 1. We use the fiber dispersion given in the manufacturer specifications [37], and assume a nonlinear coefficient of  $\gamma = 0.0011$  W<sup>-1</sup>m<sup>-1</sup>. For comparison, also propagation through a traditional 2 km fiber spool is considered where polarization effects are not compensated for.

The SOP of an optical field  $\mathbf{u} = [u_x, u_y]^T$  can be described by the Stokes vector components  $S_0 = |u_x|^2 + |u_y|^2$ ,  $S_1 = |u_x|^2 - |u_y|^2$ ,  $S_2 = 2\Re(u_x u_y^*)$ ,  $S_3 = 2\Im(u_x u_y^*)$ , and the Poincaré sphere representation is in spherical coordinates given by [16]

$$\begin{aligned}p &= \left( S_1^2 + S_2^2 + S_3^2 \right)^{1/2} S_0^{-1}, \\ \Theta &= \angle(S_1 + iS_2), \\ \Phi &= \text{asin} \left[ S_3 \left( S_1^2 + S_2^2 + S_3^2 \right)^{-1/2} \right].\end{aligned}$$

In our simulation we assume fully polarized light, i.e., the polarization degree is  $p = 1$ , and thus the polarization state is completely characterized by the two angles:  $\Theta$  describes the linear polarization direction, with  $\Theta/2$  being the orientation angle of the field.  $\Phi$  characterizes the circularity, with  $\pm 90^\circ$  denoting left and right circular polarization, respectively.

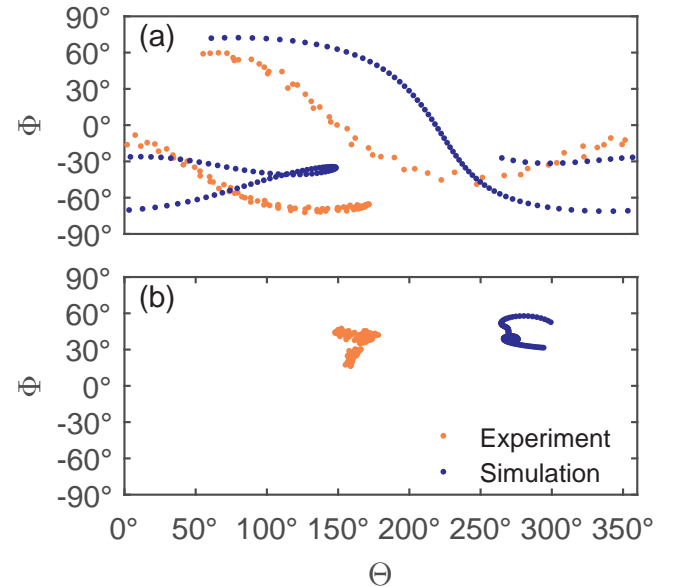


**Fig. 3.** Simulated and experimental SOP after 2 km propagation through an (a) uncompensated and (b) compensated fiber spool. The input field is wavelength-swept between 1246 – 1382 nm and is linearly polarized at  $45^\circ$  to the spool plane.

In our simulation, the stochastic nature of PMD is reflected by a random choice of the birefringence orientation angle  $\theta$  according to Eq. (14). Thus, the obtained results greatly depend on the exact realization of  $\theta$ . In Fig. 3, simulated and experimental SOP traces are shown for a wavelength sweep of 1246 – 1382 nm, with the polarization axis of the incoming field oriented at an angle of  $45^\circ$  to the spool plane. In Fig. 3(a), data for the traditional 2 km fiber spool are shown. Fig. 3(b) contains

results for the fiber system with the FRM included, consisting of the compensated 1 km spool and additionally two uncompensated 2 m spools (bending radius 3.5 cm) in front and behind it [16]. As expected, the experimental and theoretical traces do not completely coincide due to the random PMD contribution, and also because the experimental measurement setup contains some additional components not considered in the simulation, such as a circulator for the compensated spool. Furthermore, for the bending radii considered, small variations in the length of non-compensated fiber stretches on the order of 1 m can already significantly alter the position of the output SOP trajectory on the Poincaré sphere [16]. Thus, the only feature of the simulated and measured SOP trajectories that can be expected to be comparable is their extent in the  $\Theta\Phi$ -plane. Although the obtained trajectories will be different for each realization of  $\theta$ , their approximate extent is related to the PMD parameter  $D_p$ , characterizing the PMD strength and thus the mean PMD-induced deviation of the output SOP from the input SOP. We find that the extent of the computed and measured trajectories in both  $\Theta$  and  $\Phi$  is similar, confirming that the influence of birefringence on the polarization state dynamics is of comparable strength in simulation and experiment: For the uncompensated case shown in Fig. 3(a), the angular spread  $\Delta\Phi \approx 140^\circ$ , and  $\Delta\Theta$  even exceeds  $360^\circ$ . The spread is much smaller for the polarization compensated spool in Fig. 3(b), with  $\Delta\Theta \approx \Delta\Phi \approx 30^\circ$ , demonstrating the effectiveness of the polarization compensation scheme.

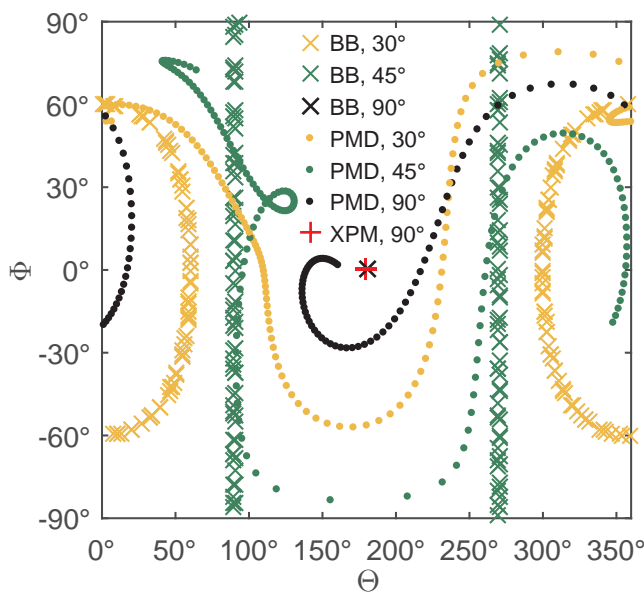


**Fig. 4.** Simulated SOP after propagation of a wavelength-swept (1246 – 1382 nm) field through an uncompensated fiber spool for different input polarization angles, taking into account only polarization effects due to bending birefringence (BB), PMD or XPM/SPM, respectively.

In Fig. 4, the simulated SOP trace for the uncompensated spool is shown, taking into account only polarization effects due to bending birefringence, PMD or XPM/SPM, respectively. For bending birefringence, the fiber spool acts as a waveplate, generally converting the linear input SOP into some elliptical SOP, as shown for a  $30^\circ$  input polarization angle. The resulting SOP trajectory is traversed several times during a wavelength sweep from 1246 – 1382 nm, corresponding to a change

in waveplate order. For a  $45^\circ$  input polarization angle, we obtain rotated linear polarization states for all wavelengths, while for  $0^\circ$  (not shown in the figure) and  $90^\circ$  the linear input SOP remains unchanged. Also PMD converts the linear input SOP into a generally elliptical SOP. In contrast to bending birefringence, the SOP trajectory is not closed, and is thus not traversed several times during a wavelength sweep. For the chosen parameters and input angles which do not approach  $0^\circ$  or  $90^\circ$ , the angular extent of the SOP traces is comparable for bending birefringence and PMD. By contrast, as exemplarily shown in Fig. 4 for an input polarization angle of  $90^\circ$ , the nonlinear effects due to XPM and SPM do not significantly alter the input SOP even for an optical power of 1 W which already exceeds typical power levels in FDML fiber spools [8].

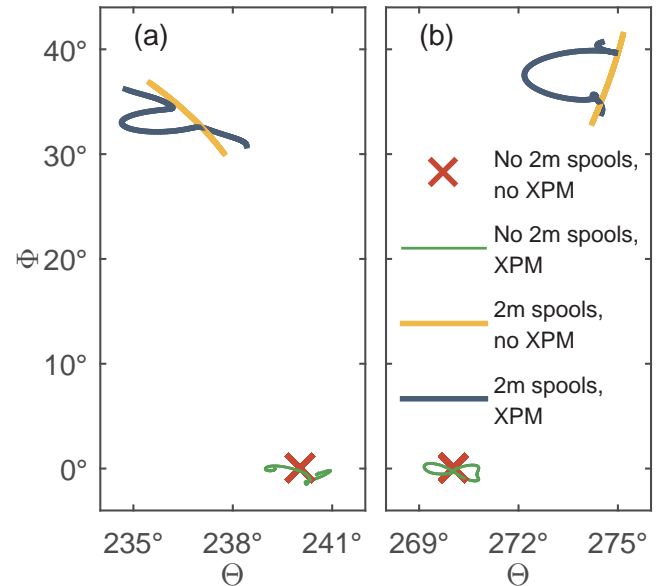


**Fig. 5.** Simulated SOP after propagation of a wavelength-swept (1246 – 1382 nm) field through the compensated fiber spool for an input polarization angle of (a)  $30^\circ$  and (b)  $45^\circ$ . Here, an ideal wavelength independent FRM is assumed. Results are shown with and without including the two uncompensated 2 m spools and fiber nonlinearities due to XPM/SPM.

In Fig. 5, the simulated SOP trace for the compensated spool is shown, assuming ideal polarization compensation by a wavelength-independent FRM. Residual polarization effects are then only due to fiber nonlinearity, i.e., XPM and SPM, as well as further, uncompensated components such as the additional 2 m spools in the measurement setup. While for ideal compensation, the input and output SOPs are identical, the fiber nonlinearity breaks the symmetry between forward and backward propagation, impeding perfect compensation of polarization effects. For an optical power of 1 W assumed here, the deviation of the output from the input SOP does however not exceed  $1.5^\circ$  in both  $\Theta$  and  $\Phi$ . As expected, the uncompensated 2 m spools alter the position of the output SOP on the Poincaré sphere, and lead to an additional angular spread of the SOP trace. By comparison of Fig. 5 with Fig. 3(b), we can see that the angular spread of the SOP traces due fiber nonlinearities or additional uncompensated 2 m spools is however much smaller than the spread due to a non-ideal FRM. This demonstrates that residual polarization effects in the compensated spool are mainly due to



the wavelength dependence of the FRM as modeled by Eq. (10), allowing optimum compensation only at the FRM design wavelength  $\lambda_F$ .

## B. FDML Laser

For FDML simulations, where the optical field is propagated over many roundtrips, the evaluation of Eq. (4) using a conventional split-step approach without precomputed matrices is computationally much slower than the numerical method developed in Section 4 where the matrices  $M_{FS}$  ( $P = 0$ ) and  $\Delta_{1,2,3}$  in Eq. (25) have to be calculated only once at the beginning of the simulation. In this case, only the numerical load for the initial computation of these matrices increases for a finer spatial discretization, i.e., a higher number  $2N$  of discrete fiber segments used (see Fig. 2). By contrast, for the conventional split-step implementation, the computation time scales with  $2N$  for every roundtrip. For a total fiber propagation distance of  $2 \times 262 \text{ m} = 524 \text{ m}$ , we obtain  $2N = 104800$  segments with a length of  $d = 0.005 \text{ m}$ . In this case, we found the numerical propagation through the fiber spool with the conventional split-step method to be about 30000 times slower than for the matrix approach with precomputed matrices. The treatment of the lumped optical elements, such as the SOA and the sweep filter, is identical in both approaches. The evaluation of the fiber propagation with precomputed matrices consumes only 20% of the computational time per roundtrip, while 80% is required for the other optical resonator elements. Consequently, for the conventional split-step method the total simulation time increases by a factor of about  $30000 \times 0.2 = 6000$ , which is prohibitive for the large number of roundtrips required for convergence.

In the following, we present simulation results for an FDML laser used for the generation of picosecond pulses [15]. The setup, illustrated in Fig. 1, is the  $4 \times$  pass configuration of Ref. [15], which is particularly interesting because it exhibits pronounced polarization effects. Here, the sweep filter center frequency is given by  $\Omega(t) = \omega_c + (\Delta\omega/2) \cos(2\pi t/T_R)$ , where  $\omega_c = 1.207 \times 10^{15} \text{ s}^{-1}$  and  $\Delta\omega = 4.083 \times 10^{13} \text{ s}^{-1}$ , corresponding to a central wavelength of 1560 nm and a sweep bandwidth of 52.75 nm. The cavity roundtrip time is  $T_R = 2.561 \mu\text{s}$ . The fiber spool ( $R_b = 0.125 \text{ m}$ ) consists of 246 m single-mode fiber combined with 16 m of dispersion compensation fiber (DCF). The chromatic dispersion is modeled based on manufacturer specifications [37] and experimental characterization data [45], respectively, and a nonlinear coefficient of  $\gamma = 0.0011 \text{ W}^{-1} \text{ m}^{-1}$  is assumed. The setup features a polarization insensitive SOA (Covega SOA1117), which is implemented as a lumped element with a frequency-dependent amplitude gain  $G_{x,y}(\omega) = \exp[\int g_{x,y}(\omega) dz]$ , obtained by integrating over the gain medium length. Additionally, we account for saturation effects by introducing a gain dependence on the input optical power  $P_{in}$  as shown in Fig. 6, modeled according to experimental characterization data. The non-instantaneous gain recovery dynamics can be considered by using a time-averaged optical power for determining the saturated gain value, e.g., in the limit of slow recovery, by averaging  $P_{in}$  over a cavity roundtrip [46]. Here we have to modify this approach since the gain recovery time  $T_L \approx 380 \text{ ps}^{-1}$  of the SOA in the investigated setup is considerably shorter than the roundtrip time, by using an exponential moving average value  $\bar{P}_{in}(t) = T_L^{-1} \int_{-\infty}^t P_{in}(\tau) \exp[-(\tau - t)/T_L] d\tau$  [18, 26]. On a discrete temporal grid with points  $t_m$  and spacing  $\Delta t$ ,  $\bar{P}_{in}(t_m)$  can then be

updated in an efficient way,

$$\bar{P}_{in}(t_m) = \bar{P}_{in}(t_{m-1}) \exp\left(-\frac{\Delta t}{T_L}\right) + \left[1 - \exp\left(-\frac{\Delta t}{T_L}\right)\right] P_{in}(t_m). \quad (27)$$

ASE is implemented as described in Section 3, adding noise and allowing the simulation to self-start [18, 26]. Furthermore, a weakly polarization dependent gain of 2 dB of the SOA module is considered in our model [16]. The ring cavity of the experimental setup contains a polarization controller, here modeled as described in Section 3D, which is in principle not required for designs with polarization insensitive SOA but can bring some performance improvement [16]. Temporal compression of the outcoupled wavelength-swept FDML light is achieved by negative dispersion, experimentally provided by a 15 km DCF which is passed four times in the  $4 \times$  pass configuration. Here, only 1.5 nm sweep range, corresponding to a sweep duration of 24 ns, is used for pulse compression in order to reduce higher order dispersion effects in the DCF [15].

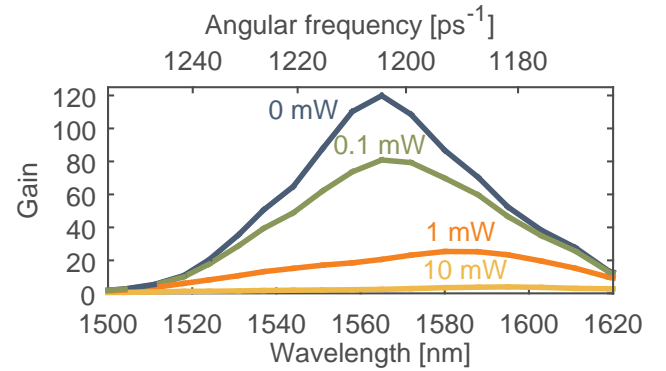


**Fig. 6.** SOA power gain  $G_x^2$  as a function of wavelength and angular frequency for various values of the incident optical power.

To ensure convergence to steady state, the pulse propagation is simulated over 500000 roundtrips, corresponding to an evolution of the optical field over 1.3 s. In analogy to the experiment, the pulse intensity profile is numerically evaluated by averaging over multiple roundtrips, which leads to a suppression of fluctuations. In our simulation, we take every 1000th roundtrip of the final 20000 roundtrips. Furthermore, we fine-tune the length of the fiber compressor so as to obtain optimum compression. To emulate the experimental conditions where the pulse width is extracted assuming a Gaussian shape [15], we determine the full width at half-maximum (FWHM) duration by performing a least-square Gaussian pulse fit to the simulated intensity profile. Similar results are obtained for the  $x$  and  $y$  components of the electric field; the simulation data presented in the following are for the total field, i.e., including both components.

In Fig. 7, a comparison of the experimental and simulated FWHM pulse widths for the  $4 \times$  pass configuration of Ref. [15] is shown as a function of the sweep filter bandwidth. As expected, a narrower filter bandwidth results in a shorter pulse, since the linewidth is reduced and thus the coherence length improves. In experiment, the filter bandwidth can however not be reduced below 110 pm due to mechanical restrictions. Here, the shortest pulse width of 68 ps is measured, which agrees very well with the numerical value of 71.4 ps obtained by the full simulation

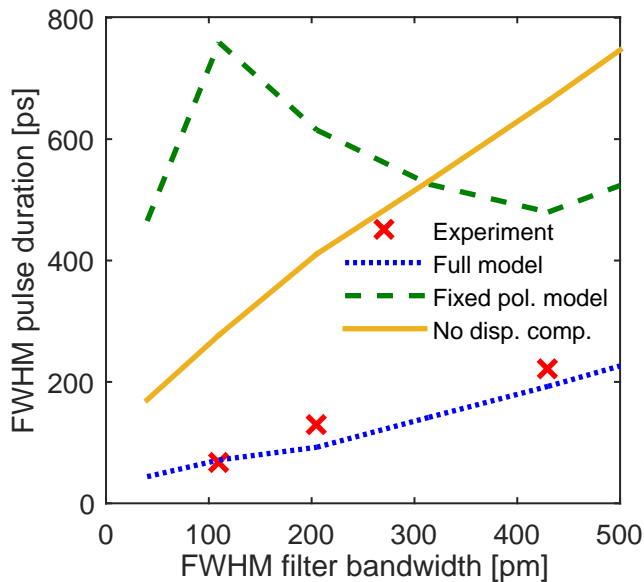


**Fig. 7.** Comparison of experimental and simulated pulse duration for the  $4\times$  pass configuration as a function of the sweep filter bandwidth. Shown are experimental data [15], along with simulation results obtained by the full simulation approach of Section 4 and the fixed polarization model developed for PM FDML lasers [18]. Additionally, full simulation data for a laser setup without dispersion compensation is displayed.

approach of Section 4. Very good agreement between experiment and theory is also found for the other sweep filter bandwidths investigated. In contrast, the model assuming fixed polarization as obtained for a PM configuration [18] yields much longer pulse durations, e.g., 759.2 ps at a filter bandwidth of 110 pm, exceeding the measured value by a factor of more than 10. Experimentally, the instantaneous linewidth (averaged over a sweep) is estimated to be around 10 pm, which is more than a factor of 10 below the filter bandwidth. Due to the very high sweep speed, an indirect measurement technique is used, based on evaluating the interference signal from a Michelson interferometer [15]. By contrast, in the simulation the instantaneous linewidth can directly be determined by Fourier transforming the field envelope defined in Eq. (3), since here the frequency axis moves along with the sweep filter center frequency and smearing of the lineshape due to the sweep filter dynamics is thus avoided [25, 26]. An FWHM instantaneous linewidth of 7.44 pm is obtained for the full simulation in reasonable agreement with the experimental estimate, given the uncertainty of the measurement. The fixed polarization model yields 46.8 pm linewidth, implying a much lower coherence and substantially reduced compressibility of the optical field, and thus resulting in much longer pulses than obtained by the experiment and full simulation. This demonstrates that FDML operation is significantly affected by polarization effects, leading to considerably improved coherence for setups with polarization insensitive SOA where the polarization dynamics can freely unfold. More detailed simulations show that over a wide parameter range, the obtained pulse duration and linewidth only weakly depend on the exact value of bending birefringence, PMD and XPM as quantified by  $\Delta\beta_b$ ,  $\Delta\beta_{\text{PMD}}$  and  $\gamma$  in Eq. (4). Also assuming an ideal FRM, as done in Fig. 5, does not change the simulation re-

sults significantly. By contrast, the amount of residual intracavity dispersion plays an important role, and thorough dispersion compensation is crucial to obtain short pulses. For illustration, simulation results for an uncompensated FDML setup are included in Fig. 7, where the 16 m DCF is replaced by a normal SMF. The obtained pulse durations, as well as the corresponding linewidths, are larger by a factor of  $\sim 3-4$  as compared to the full simulation results for the dispersion compensated setup.

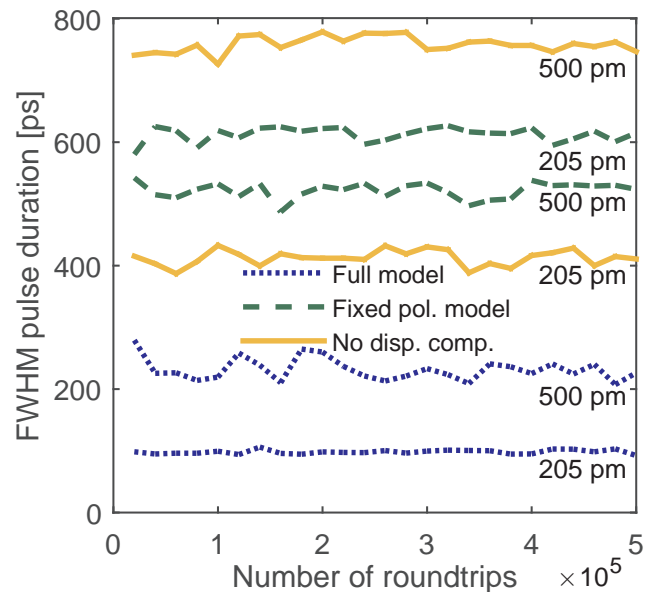


**Fig. 8.** Simulated pulse duration for the  $4\times$  pass configuration as a function of the roundtrip number for sweep filter bandwidths of 205 pm and 500 pm, respectively.

To ensure convergence of the simulation results of Fig. 7, the computed pulse duration is displayed in Fig. 8 as a function of the roundtrip number for the full simulation approach with and without dispersion compensation, as well as for the fixed polarization model. Again, for each datapoint we average over 20 pulses, considering every 1000th of 20000 successive roundtrips. Apart from small variations due to the sweep-to-sweep jitter [47], the pulse duration does not change significantly anymore after a few 100000 roundtrips or less, depending on the laser parameters.

All in all, the simulation results of Fig. 7 substantiate experimental observations that low residual intracavity dispersion is crucial for high-coherence operation of FDML lasers [15, 48], and that the smallest linewidths down to a few pm are obtained for non-PM configurations with polarization insensitive SOA.

## 6. CONCLUSION

In conclusion, the paper provides a theoretical model and its efficient numerical implementation for the simulation of wavelength-swept waveform propagation in optical fiber systems, including the polarization dynamics in fiber spools and other polarization dependent optical components. We demonstrate that this approach allows for a realistic simulation of non-PM FDML operation over several  $10^5$  roundtrips, yielding good agreement with experimental data. The simulation approach is used to investigate the influence of polarization effects such as bending birefringence, PMD and XPM on the

wavelength-swept waveform propagation in fiber spools and on FDML laser operation. The simulation results substantiate experimental observations that high-coherence operation of FDML lasers requires low residual intracavity dispersion, and that the smallest linewidths down to a few pm are obtained for non-PM configurations with polarization insensitive SOA. The developed numerical model can also be of general relevance for tunable lasers which use external fiber delay spools to increase the wavelength sweep speed in applications such as OCT [49, 50].

**Funding.** Deutsche Forschungsgemeinschaft (DFG) (JI 115/4-1, JI 115/8-1, HU 1006/6); European Union project ENCOMOLE-2i (Horizon 2020, ERC CoG no. 646669).

## REFERENCES

- D. Huang, E. A. Swanson, C. P. Lin, J. S. Schuman, W. G. Stinson, W. Chang, M. R. Hee, T. Flotte, K. Gregory, C. A. Puliafito, and J. G. Fujimoto, "Optical coherence tomography," *Science* **254**, 1178–1181 (1991).
- C. Jirauschek and R. Huber, "Wavelength shifting of intra-cavity photons: Adiabatic wavelength tuning in rapidly wavelength-swept lasers," *Biomed. Opt. Express* **6**, 2448–2465 (2015).
- R. Huber, M. Wojtkowski, and J. G. Fujimoto, "Fourier Domain Mode Locking (FDML): A new laser operating regime and applications for optical coherence tomography," *Opt. Express* **14**, 3225–3237 (2006).
- K. Hsu, P. Meemon, K.-S. Lee, P. J. Delfyett, and J. P. Rolland, "Broadband Fourier-domain mode-locked lasers," *Photon. Sens.* **1**, 222–227 (2011).
- R. Huber, D. C. Adler, and J. G. Fujimoto, "Buffered Fourier domain mode locking: unidirectional swept laser sources for optical coherence tomography imaging at 370,000 lines/s," *Opt. Lett.* **31**, 2975–2977 (2006).
- W. Wieser, B. R. Biedermann, T. Klein, C. M. Eigenwillig, and R. Huber, "Multi-megahertz OCT: High quality 3D imaging at 20 million A-scans and 4.5 GVoxels per second," *Opt. Express* **18**, 14685–14704 (2010).
- T. Klein, W. Wieser, C. M. Eigenwillig, B. R. Biedermann, and R. Huber, "Megahertz OCT for ultrawide-field retinal imaging with a 1050nm Fourier domain mode-locked laser," *Opt. Express* **19**, 3044–3062 (2011).
- Y. Mao, C. Fluerau, S. Sherif, and S. Chang, "High performance wavelength-swept laser with mode-locking technique for optical coherence tomography," *Opt. Commun.* **282**, 88–92 (2009).
- D. C. Adler, W. Wieser, F. Trepanier, J. M. Schmitt, and R. A. Huber, "Extended coherence length Fourier domain mode locked lasers at 1310 nm," *Opt. Express* **19**, 20930–20939 (2011).
- D. C. Adler, Y. Chen, R. Huber, J. Schmitt, J. Connolly, and J. G. Fujimoto, "Three-dimensional endomicroscopy using optical coherence tomography," *Nature Photon.* **1**, 709–716 (2007).
- E. J. Jung, C.-S. Kim, M. Y. Jeong, M. K. Kim, M. Y. Jeon, W. Jung, and Z. Chen, "Characterization of FBG sensor interrogation based on a FDML wavelength swept laser," *Opt. Express* **16**, 16552–16560 (2008).
- B. C. Lee and M. Y. Jeon, "Remote fiber sensor based on cascaded Fourier domain mode-locked laser," *Opt. Commun.* **284**, 4607–4610 (2011).
- B. C. Lee, E.-J. Jung, C.-S. Kim, and M. Y. Jeon, "Dynamic and static strain fiber Bragg grating sensor interrogation with a 1.3  $\mu\text{m}$  Fourier domain mode-locked wavelength-swept laser," *Meas. Sci. Technol.* **21**, 094008 (2010).
- S. Karpf, M. Eibl, W. Wieser, T. Klein, and R. Huber, "A time-encoded technique for fibre-based hyperspectral broadband stimulated Raman microscopy," *Nat. Commun.* **6**, 6784 (2015).
- C. M. Eigenwillig, W. Wieser, S. Todor, B. R. Biedermann, T. Klein, C. Jirauschek, and R. Huber, "Picosecond pulses from wavelength-swept continuous-wave Fourier domain mode-locked lasers," *Nat. Commun.* **4**, 1848 (2013).
- W. Wieser, G. Palte, C. M. Eigenwillig, B. R. Biedermann, T. Pfeiffer, and R. Huber, "Chromatic polarization effects of swept waveforms in FDML lasers and fiber spools," *Opt. Express* **20**, 9819–9832 (2012).
- C. Jirauschek and R. Huber, "Modeling and analysis of polarization effects in Fourier domain mode-locked lasers," *Opt. Lett.* **40**, 2385–2388 (2015).
- C. Jirauschek, B. Biedermann, and R. Huber, "A theoretical description of Fourier domain mode locked lasers," *Opt. Express* **17**, 24013–24019 (2009).
- S. Slepneva, B. Kelleher, B. O'Shaughnessy, S. P. Hegarty, A. G. Vladimirov, and G. Huyet, "Dynamics of Fourier domain mode-locked lasers," *Opt. Express* **21**, 19240–19251 (2013).
- C. Tu, Y. Deng, M. Cai, Z. Huang, Y. Li, F. Lu, and E. Li, "Theoretical study on instantaneous linewidth of Fourier-domain mode-locked fiber lasers," *Opt. Commun.* **285**, 5287–5292 (2012).
- F. Li, J. Nathan Kutz, and P. Wai, "WKB analysis of Fourier domain mode locked fiber lasers," in "Conference on Lasers and Electro-Optics/Pacific Rim," (Optical Society of America, 2013), p. WPA\_26.
- M. Bonesi, H. Sattmann, T. Torzicky, S. Zotter, B. Baumann, M. Pircher, E. Götzinger, C. Eigenwillig, W. Wieser, R. Huber, and C. K. Hitzenberger, "High-speed polarization sensitive optical coherence tomography scan engine based on Fourier domain mode locked laser," *Biomed. Opt. Express* **3**, 2987–3000 (2012).
- M. Bonesi, H. Sattmann, T. Torzicky, S. Zotter, B. Baumann, M. Pircher, E. Götzinger, C. Eigenwillig, W. Wieser, R. Huber, and C. K. Hitzenberger, "High-speed polarization sensitive optical coherence tomography scan engine based on Fourier domain mode locked laser: erratum," *Biomed. Opt. Express* **4**, 241–244 (2013).
- G. Palte, W. Wieser, B. R. Biedermann, C. M. Eigenwillig, and R. Huber, "Fourier domain mode locked (FDML) lasers for polarization sensitive OCT," in "Proc. SPIE 7372, Optical Coherence Tomography and Coherence Techniques IV," (2009), p. 73720M.
- S. Todor, B. Biedermann, W. Wieser, R. Huber, and C. Jirauschek, "Instantaneous lineshape analysis of Fourier domain mode-locked lasers," *Opt. Express* **19**, 8802–8807 (2011).
- S. Todor, B. Biedermann, R. Huber, and C. Jirauschek, "Balance of physical effects causing stationary operation of Fourier domain mode-locked lasers," *J. Opt. Soc. Am. B* **29**, 656–664 (2012).
- S. Marschall, T. Torzicky, T. Klein, W. Wieser, M. Pircher, E. Götzinger, S. Zotter, M. Bonesi, B. Biedermann, C. Pedersen, R. Huber, C. Hitzenberger, and P. Andersen, "High-speed polarization-sensitive OCT at 1060 nm using a Fourier domain mode-locked swept source," in "Proc. SPIE 8427, Biophotonics: Photonic Solutions for Better Health Care III, 84271D," (2012), p. 84271D.
- G. Agrawal, *Nonlinear Fiber Optics* (Academic, 2001).
- P. K. A. Wai and C. R. Menyuk, "Polarization decorrelation in optical fibers with randomly varying birefringence," *Opt. Lett.* **19**, 1517–1519 (1994).
- P. K. A. Wai and C. R. Menyuk, "Polarization mode dispersion, decorrelation, and diffusion in optical fibers with randomly varying birefringence," *J. Lightwave Technol.* **14**, 148–157 (1996).
- H. S. Lee, E. J. Jung, S. N. Son, M. Y. Jeong, and C. S. Kim, "FDML wavelength-swept fiber laser based on EDF gain medium," in "14th OptoElectronics and Communications Conference," (IEEE, 2009), p. FA5.
- T. Klein, W. Wieser, B. R. Biedermann, C. M. Eigenwillig, G. Palte, and R. Huber, "Raman-pumped Fourier-domain mode-locked laser: analysis of operation and application for optical coherence tomography," *Opt. Lett.* **33**, 2815–2817 (2008).
- D. Cassioli, S. Scotti, and A. Mecozzi, "A time-domain computer simulator of the nonlinear response of semiconductor optical amplifiers," *IEEE J. Quant. Electron.* **36**, 1072–1080 (2000).
- R. Ulrich, S. Rashleigh, and W. Eickhoff, "Bending-induced birefringence in single-mode fibers," *Opt. Lett.* **5**, 273–275 (1980).
- Y. Namihira, "Opto-elastic constant in single mode optical fibers," *J. Lightwave Technol.* **3**, 1078–1083 (1985).
- D. C. Hurlley and J. A. Turner, "Measurement of Poisson's ratio with contact-resonance atomic force microscopy," *J. Appl. Phys.* **102**, 033509 (2007).

37. Corning, *Corning SMF-28 Optical Fiber Product Information* (2002).
38. J.-I. Sakai and T. Kimura, "Birefringence caused by thermal stress in elliptically deformed core optical fibers," *IEEE J. Quant. Electron.* **18**, 1899–1909 (1982).
39. H.-D. Rudolph and E.-G. Neumann, "Approximations for the eigenvalues of the fundamental mode of a step index glass fiber waveguide," *Nachrichtentechnische Zeitschrift* **29**, 328–329 (1976).
40. F. A. Jenkins and H. E. White, *Fundamentals of Optics* (McGraw-Hill, 1976).
41. N. P. Barnes and L. B. Petway, "Variation of the Verdet constant with temperature of terbium gallium garnet," *J. Opt. Soc. Am. B* **9**, 1912–1915 (1992).
42. Granopt, Japan, *Technical manual No.G005-E, Faraday Rotator (Rare-earth Iron Garnet single crystals)* (2013).
43. Northrop Grumman, "Terbium gallium garnet - TGG," (2011). [www.northropgrumman.com/BusinessVentures/SYNOPTICS/Products/SpecialtyCrystals/Documents/pageDocs/TGG.pdf](http://www.northropgrumman.com/BusinessVentures/SYNOPTICS/Products/SpecialtyCrystals/Documents/pageDocs/TGG.pdf), accessed May 3, 2016.
44. M. Presi and E. Ciaramella, "Stable self-seeding of reflective-SOAs for WDM-PONs," in "Optical Fiber Communication Conference," (Optical Society of America, 2011), p. OMP4.
45. W. Wieser, B. R. Biedermann, T. Klein, C. M. Eigenwillig, and R. Huber, "Ultra-rapid dispersion measurement in optical fibers," *Opt. Express* **17**, 22871–22878 (2009).
46. S. Wang, A. Docherty, B. S. Marks, and C. R. Menyuk, "Comparison of numerical methods for modeling laser mode locking with saturable gain," *J. Opt. Soc. Am. B* **30**, 3064–3074 (2013).
47. B. R. Biedermann, W. Wieser, C. M. Eigenwillig, T. Klein, and R. Huber, "Direct measurement of the instantaneous linewidth of rapidly wavelength-swept lasers," *Opt. Lett.* **35**, 3733–3735 (2010).
48. B. R. Biedermann, W. Wieser, C. M. Eigenwillig, T. Klein, and R. Huber, "Dispersion, coherence and noise of Fourier domain mode locked lasers," *Opt. Express* **17**, 9947–9961 (2009).
49. Y.-J. Hong, S. Makita, S. Sugiyama, and Y. Yasuno, "Optically buffered Jones-matrix-based multifunctional optical coherence tomography with polarization mode dispersion correction," *Biomed. Opt. Express* **6**, 225–243 (2015).
50. B. Potsaid, B. Baumann, D. Huang, S. Barry, A. E. Cable, J. S. Schuman, J. S. Duker, and J. G. Fujimoto, "Ultrahigh speed 1050nm swept source/Fourier domain OCT retinal and anterior segment imaging at 100,000 to 400,000 axial scans per second," *Opt. Express* **18**, 20029–20048 (2010).